Materials Horizons

Semiconductor to Topological Insulator Transition Induced by Stress Propagation in Metal Dichalcogenides Core-Shell Lateral Heterostructures

Journal:	*Materials Horizons*
Manuscript ID	MH-COM-10-2020-001688.R1
Article Type:	Communication
Date Submitted by the Author:	11-Dec-2020
Complete List of Authors:	Dong, Xi; Michigan State University, Physics and Astronomy Lai, Wei; Michigan State University, Chemical Engineering & Materials Science Zhang, Pengpeng; Michigan State University, Physics and Astronomy

Conceptual insights

Phase engineering enables the incorporation of materials with selective properties associated with the different polymorphic phases into devices for various applications. In light of integrating rational heterostructure design and phase engineering in one step, we demonstrate a novel phase transition technique based on the construction of lateral (WSe_2/$SnSe_2$) core-shell architecture, which is distinct from any of the known phase transition protocols. Since the proposed mechanism only fundamentally requires a van der Waals interacting substrate and sufficient core-shell lattice mismatch, our approach should be uniquely versatile towards other transition metal dichalcogenides and chemical vapor deposition methods. Compared to the conventional phase transition methods, it is also less likely to introduce structural damage, contaminations, or unwanted substrate perturbation. Most importantly, the rationally designed topological insulator/superconductor (1T'-WSe_2/1T-$SnSe_2$) lateral heterostructure with the exposed boundary on surface provides an ideal platform for future investigations into spatial extension of superconducting proximity effect and induced topological superconductivity at the edge of 2D topological insulator.

Phase transformation of WSe_2 upon formation of enclosed core-shell lateral heterostructure with $SnSe_2$

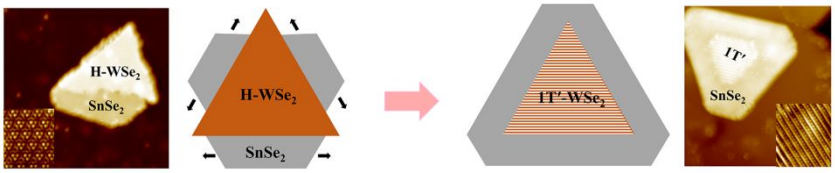

ARTICLE

Semiconductor to Topological Insulator Transition Induced by Stress Propagation in Metal Dichalcogenides Core-Shell Lateral Heterostructures

Received 00th January 20xx,
Accepted 00th January 20xx

DOI: 10.1039/x0xx00000x

Xi Dong, [a] Wei Lai [b] and Pengpeng Zhang *[a]

Polymorphic phase transition is an important route for engineering the properties of two-dimensional materials. Heterostructure construction, on the other hand, not only allows the integration of different functionalities for device applications, but also enables the exploration of new physics arising from proximity coupling. Yet, implementing a design that incorporates the advantages of both remains underexplored. Here, based on comprehensive experimental and theoretical studies of $WSe_2/SnSe_2$ core-shell lateral heterostructure, we demonstrate an unexpected H to T′ phase transition in transition metal dichalcogenides (TMDs), correlating to a change of materials properties from semiconductor to topological insulator (TI), and propose a novel shell-to-core stress propagation mechanism. This finding offers new insights into TMD phase transition empowered by the rational design of heterostructures. Owing to the superconducting properties of $SnSe_2$ at low temperatures, the unique TI/superconductor core-shell template is expected to add more arsenals to the ongoing search of Majorana fermions in condensed matter systems.

Introduction

Two-dimensional (2D) materials exhibit a wide variety of remarkable properties that can be incorporated into device platform via construction of heterostructures (HSs).[1-4] From fundamental perspectives, HSs offer unique opportunities to tune the properties of individual constituents[5] or even to induce new features associated with proximity coupling.[6] Among 2D materials, transition metal dichalcogenides (TMDs) with electronic and optical properties strongly tied to the number of layers[7], polymorphic phases of monolayers and their stacking have received enormous attention.[8] Phase engineering and integration of desired functionalities into HSs are of paramount interests in TMD research,[1, 8] which become even more compelling with recent discoveries of topological properties in the distorted octahedral phase (T′-phase) of some group VI TMDs.[9-13] In HSs composed of these T′-phase TMDs and conventional superconductors, topological superconductivity could emerge to host Majorana fermions for fault-tolerant quantum computing.[14, 15]

Nonetheless, except for 1T′-WTe_2, T′-phase of group VI TMDs are metastable[16] and thus remain difficult to access,[8] creating additional barriers for HSs integration. Direct synthesis is typically carried out at conditions far from equilibrium,[17] restricting the quality, e.g., domain size of the film, whereas phase transition triggered by mechanical stress or electron doping might introduce structural damage[18] and/or additional source of contamination.[19] As substrate is the indispensable part of devices, substrate-induced phase transition has also been explored, mainly attributed to interfacial charge transfer arising from the strong/hybridizing interaction at the interface, which unavoidably amounts to large electronic perturbation.[20] To better control electronic properties and to readily incorporate with HSs, it is imperative to develop more robust and versatile phase engineering methodologies that put less constraints on the choice of substrates or the heteroepitaxial design.

In this work, we demonstrate a novel technique that combines the phase engineering and HS construction in one step. H to T′ phase transition is realized in WSe_2 upon the bottom-up construction of $WSe_2/SnSe_2$ core-shell lateral HS by molecular beam epitaxy (MBE). Scanning tunneling microscopy/spectroscopy (STM/STS) and first-principles studies reveal the semiconductor to topological insulator (TI) transition associated with the polymorphic change of WSe_2 and exclude electron doping as the origin of phase transition. In addition to the observation of misfit dislocations which relax the epitaxial strain at heterojunctions,[21, 22] we propose a novel phase transition mechanism that involves the propagation of stress from shell to core mediated through the covalently bonded core-shell boundaries. Topological edge state is proved to be robust against local perturbations from misfit dislocations. Since $SnSe_2$ becomes superconducting at low temperatures,

[a] Department of Physics and Astronomy, Michigan State University, East Lansing, MI 48824, USA
[b] Department of Chemical Engineering and Materials Science, Michigan State University, East Lansing, MI 48824, USA
*Corresponding author: zhangpe@msu.edu
† Footnotes relating to the title and/or authors should appear here.
Electronic Supplementary Information (ESI) available: [Methods, apparent height measurement, band edge identification, calculated PDOS and STS comparison, structural description, complications of MBE deposition, topological edge state at defected areas]. See DOI: 10.1039/x0xx00000x

$WSe_2/SnSe_2$ lateral HS with the directly exposed boundary on surface provides a valuable platform for future investigations into topological superconductivity and spatial extent of proximity coupling.

Results and discussion

Observation of H to T′ phase transition in WSe_2 core

$WSe_2/SnSe_2$ core-shell architectures were grown on highly oriented pyrolytic graphite (HOPG) via sequential MBE deposition of WSe_2 and $SnSe_2$ (see Methods of ESI† for details). Thermodynamically stable H-phase of WSe_2 was formed initially, with substrate held at ~723K,[23] as confirmed by the lattice measurements shown in the inset of Fig. 1(a).[24] For the subsequent $SnSe_2$ deposition, substrate temperature was lowered to ~438K to avoid the decomposition of $SnSe_2$ and the formation of alloy. Inset of Fig. 1(b) reveals atomically resolved 1T-$SnSe_2$ that preferentially nucleates along the edges of existing WSe_2 islands. Intriguingly, approaching the formation of enclosed architecture, characteristic stripe-like features emerge on WSe_2 core (Fig. 1 (c-e)). These lateral heterostructures that are composed of a WSe_2 inner "core" and a $SnSe_2$ outer "shell" are termed core-shell architecture in this article (See more information in Section 1 of ESI†). The striped phase with structure illustrated in the inset of Fig. 1(e) is commonly referred to as T′-phase,[11, 12] suggesting a H to T′ phase transition in WSe_2 core. The observed phase transition is closely related to the degree of $SnSe_2$ coverage surrounding H-WSe_2 islands, as depicted in the schematics in Fig. 1(f-i), but is likely independent of the substrate as the T′-phase is identified on both HOPG (Fig. 1(d)) and 1H-WSe_2/HOPG (Fig. 1(e)). As mentioned earlier, phase transition can be triggered by mechanical stress[18] or electron doping.[19, 20] Both need to be considered since the coverage-dependent trend could be associated with the increase in either charge transfer or strain at the core-shell boundary.

Investigation of charge transfer behaviors by STM/STS

We first examine the charge transfer behaviors in the system prior to phase transition, i.e. 1H-WSe_2:1T-$SnSe_2$ (1H/1T) lateral HS on HOPG. H to T′ phase transition in the scheme of charge transfer requires excess electrons, i.e., electron doping. Metastable T′ phase of group VI TMDs has a higher total energy than the stable H phase,[16] however, the conduction band minimum (CBM) of T′ phase lies in a much lower energy level than that of the H phase, originating from the *d*-orbital arrangement.[25] Thus, injection of excessive electrons is expected to bring the total energy of H phase above that of T′ phase, inducing phase transition by switching the ground state to T′.[26] Since the 1H/1T HS is anticipated to reach charge equilibrium with the underlying substrate, interfacial band alignment needs to be established. As depicted in Fig. S2 of ESI†, STS curves taken on the interior of 1H-WSe_2 and 1T-$SnSe_2$ domains far from the lateral boundary agree well with the previous reports of the respective pristine monolayers on graphene.[27, 28] The extracted quasiparticle bandgap (~2.50eV) for 1H-WSe_2 is significantly larger than the optical bandgap

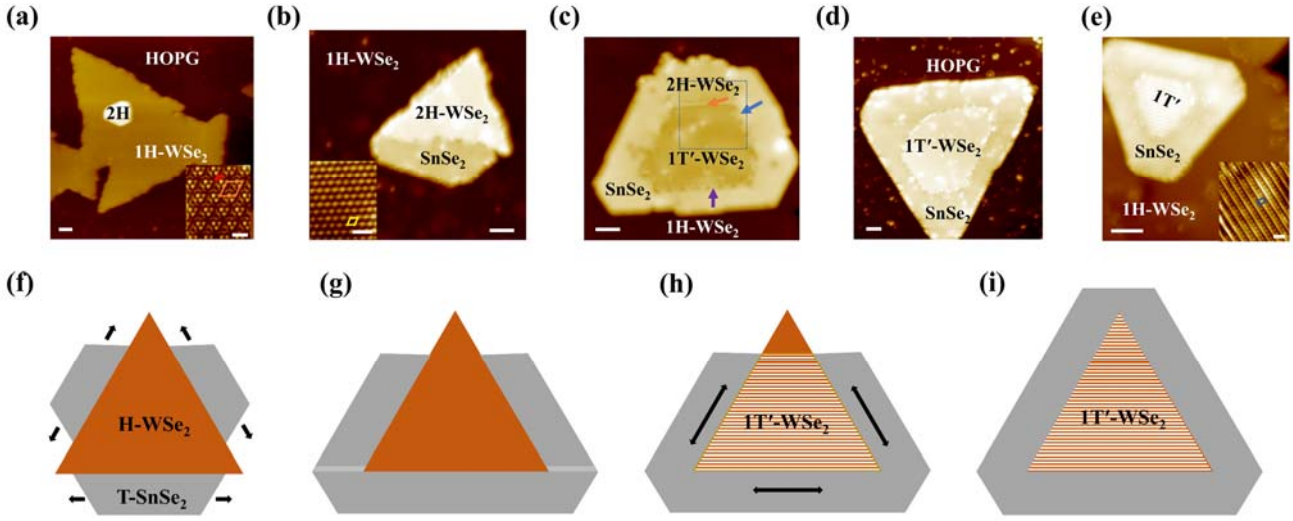

Figure 1. Phase transition in $SnSe_2$-surrounded WSe_2 islands. (a) STM image of H-WSe_2 grown on HOPG (V_s=1.5V, I_t=5pA). Inset: Atomically resolved image of 1H-WSe_2 (V_s=1.3V, I_t=30pA). Red and brown rhombic depict the unit cells of 1H-WSe_2 and the (3×3) Moiré pattern of 1H-WSe_2 on HOPG, respectively. (b) $SnSe_2$ preferentially nucleated along the edges of WSe_2 island (V_s=-2.0V, I_t=30pA). Inset: Atomically resolved image of 1T-$SnSe_2$ (V_s=1.3V, I_t=30pA). Yellow rhombic marks the unit cell. Lattice constants are measured to be $a_1 = b_1 = 0.33 \pm 0.02$ nm, $\alpha_1 = 58^\circ \pm 2^\circ$ for 1H-WSe_2 and $a_2 = b_2 = 0.39 \pm 0.02$ nm, $\alpha_2 = 57^\circ \pm 2^\circ$ for 1T-$SnSe_2$. (c) Incomplete H to T′ phase transition when WSe_2 island is not fully surrounded by $SnSe_2$ (V_s=2V, I_t=30pA, 5nm scale bar). Orange arrow marks boundary between the H- and T′-phases of WSe_2. Blue and purple arrows label arc-like features at the boundaries between 1T′-WSe_2 and 1T-$SnSe_2$. The dashed box depicts an area that will be zoomed in Fig. 5(a). (d-e) 1T′-WSe_2 (core)/1T-$SnSe_2$ (shell) HSs on: (d) HOPG (V_s=1.5V, I_t=5pA) and (e) 1H-WSe_2/HOPG (V_s=1.6V, I_t=30pA). Inset: Atomically resolved image of 1T′-WSe_2 (V_s=-0.1V, I_t=100pA). Blue rectangle illustrates the unit cell, with the lattice constants of $a = 0.34 \pm 0.02$ nm, $b = 0.60 \pm 0.02$ nm, and $\alpha = 88^\circ \pm 2^\circ$. (f-i) Schematics of structural evolution correlating to the STM images with increasing shell coverage. Light grey in (g) depicts the shell merging front. Black double arrows in (h) illustrate the direction of shear stress and gliding motion. Scale bars: 1nm for insets and 5nm for others.

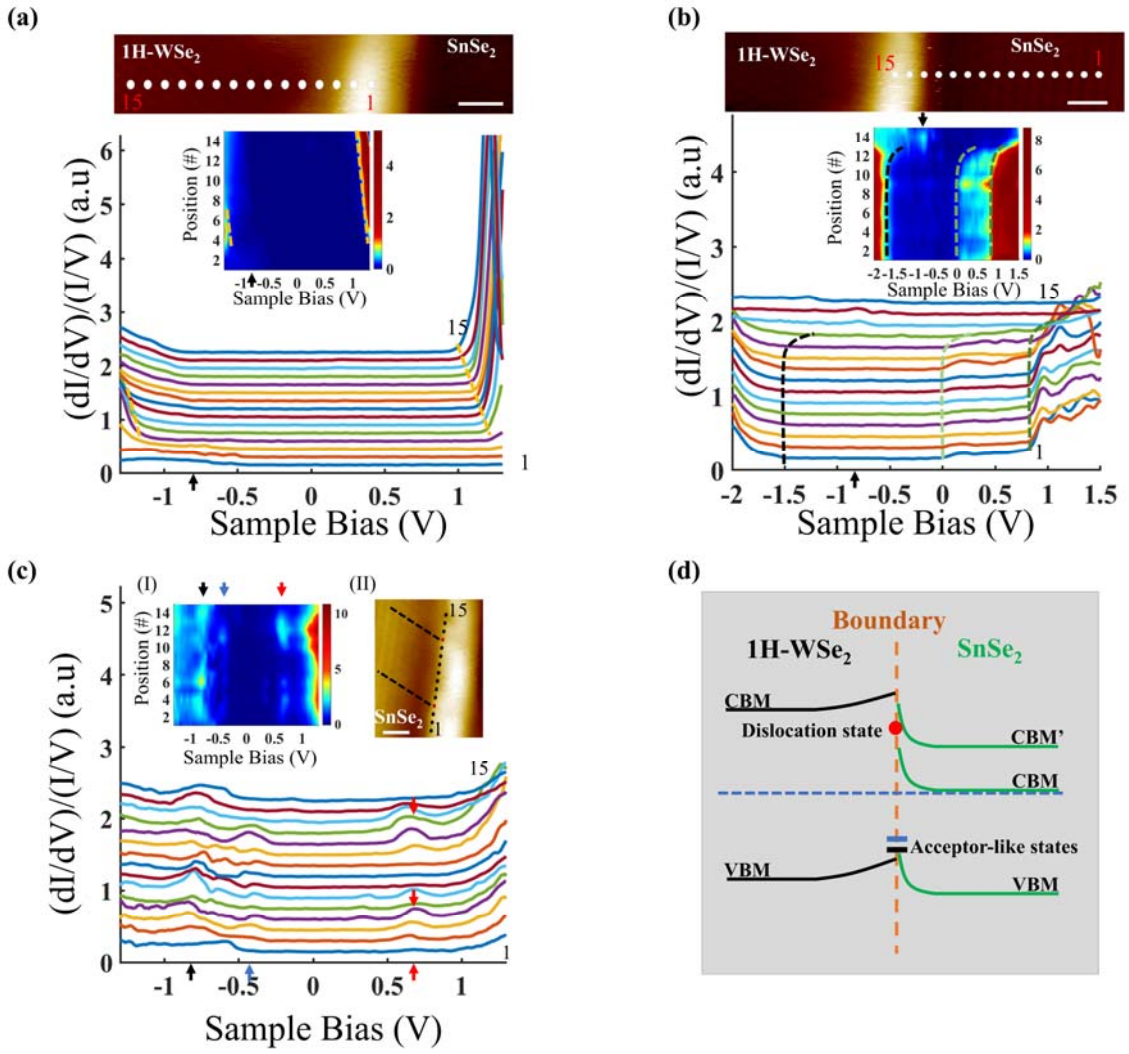

Figure 2. Electronic structures and band bending behavior near boundaries of 1H-WSe_2 and 1T-$SnSe_2$. (a-c) Vertically offset normalized dI/dV spectra taken on the 15 equally spaced points from the interior of 1H-WSe_2 or 1T-$SnSe_2$ to the boundary and along the boundary as marked on the respective STM images. Insets: Density of states (DOS) heatmap with x-axis, y-axis, and color representing sample bias, point number, and (dI/dV)/(I/V), respectively. In (a), towards the boundary (point 15 to point 1), a gradual upward band bending is identified in the WSe_2 domain by tracing the shifts of band edges (orange dashed lines) on both the spectra and heatmap. In (b), three distinct spectra features associated with the electronic structure of $SnSe_2$ are revealed, corresponding to VBM (black trace), CBM (light green trace) and CBM' (dark green trace). A steep upward band bending is observed near the boundary. In (c), acceptor-like states at the negative sample bias, as highlighted by black and blue arrows, persist throughout the entire boundary. Meanwhile, the intensity of the peak at ~0.65V (red arrows) is spatially modulated, which is expected to correlate to misfit dislocations. Specifically, the red dots in STM image (inset II) mark the locations (points 4 &12) of the maximum peak intensity at ~0.65V, which corresponds to a distance of 6 times $SnSe_2$ lattice constant (~2.30nm) by tracing along the high symmetry direction in $SnSe_2$ domain (black dashed lines). (d) Schematic diagram to illustrate the generic band alignment and the evolution of CBM and VBM energy levels with respect to the physical position towards the 1H-WSe_2/1T-$SnSe_2$ boundary. Setpoint for normalized dI/dV spectra (V_s=-1.3V, I_t=200pA). Bias for STM images (V_s=-1.3V, I_t=30pA). Scale bars: 1nm.

(~1.60eV)[29] which is mainly attributed to the large exciton binding energy.[30, 31] Meanwhile, the insensitivity of STS to electronic states of large parallel momentum could also contribute to the overestimation of quasiparticle bandgap (See more information in Section 2 of ESI†). 1H-WSe_2 appears to be nearly charge neutral with Fermi level residing at the middle of the bandgap. Thus, phase transition is unlikely the result of interfacial charge transfer with substrate. On the other hand, due to the relatively high work function of $SnSe_2$ (~5.3eV),[32] electrons are transferred from HOPG to $SnSe_2$, pulling its CBM down to the Fermi level.

After establishing band alignment with the substrate, we explore the charge transfer behaviors across the 1H/1T lateral heterojunction by extrapolating the band structure evolution towards the boundary using spatially resolved STS. As illustrated in the vertically offset STS curves and the corresponding density of states (DOS) heatmaps in Fig. 2 (a-b), a clear upward band bending is witnessed on both sides of the boundary by tracing the onsets of valence band maximum (VBM) and CBM. This indicates that electrons are depleted from both domains and accumulated at the boundary, which renders electron doping an unlikely origin of the phase transition observed in this study.

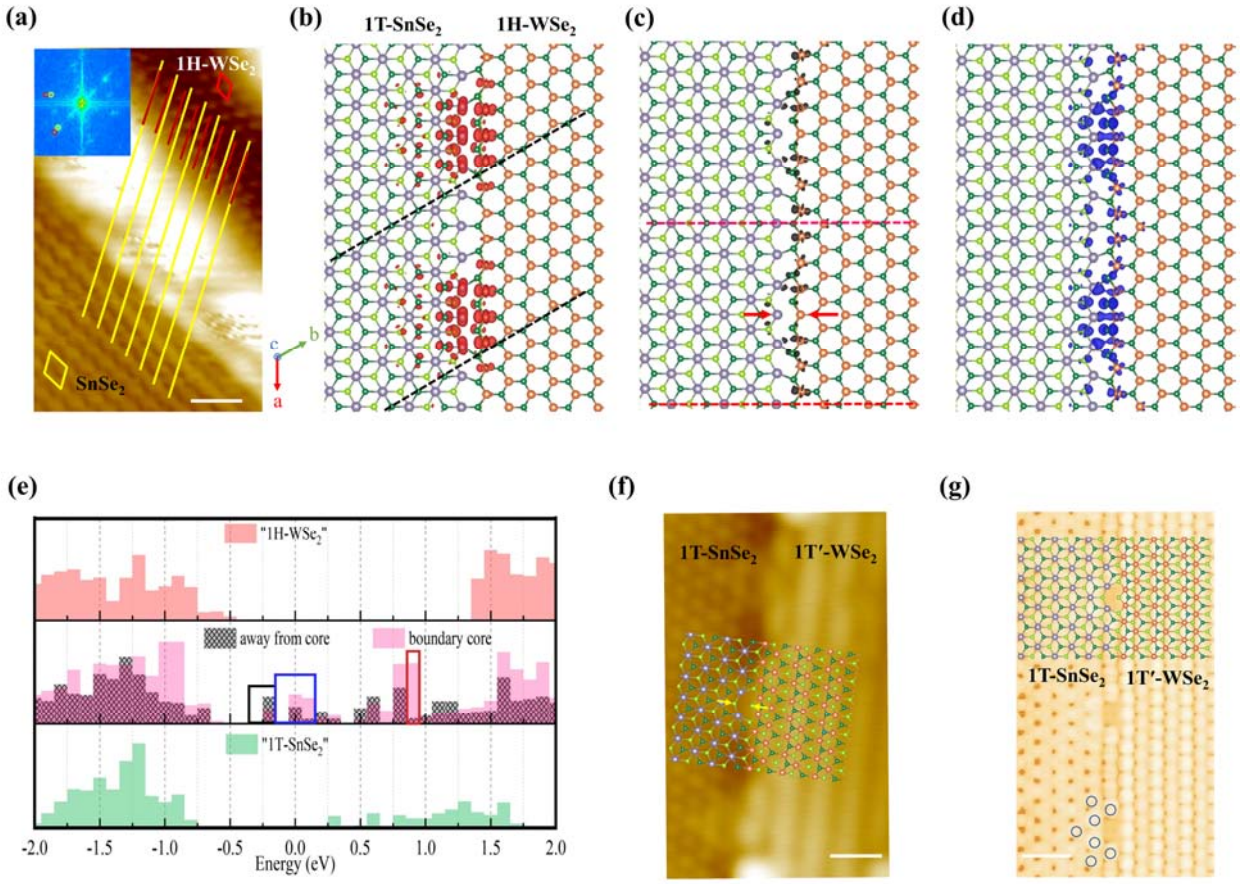

Figure 3. Impacts of misfit dislocation on morphologies and electronic states of 1H-WSe_2/1T-$SnSe_2$ and 1T′-WSe_2/1T-$SnSe_2$ boundaries. (a) STM image (V_s=-1.3V, I_t=100pA) of 1H-WSe_2/1T-$SnSe_2$ lateral HS grown on HOPG. Unit cells of the two domains are labelled by the red and yellow rhombic, respectively. Inset: fast Fourier transformation (FFT) of the STM image, where the red and yellow circles correspond to the diffraction spots of WSe_2 and $SnSe_2$ lattices, respectively. 1H-WSe_2 and 1T-$SnSe_2$ domains are azimuthally aligned within the experimental error, evidenced by the STM image and its FFT. (b-d) Simulated atomic structure and charge density plots in the energy ranges of: (b) 0.9 – 1.0 eV, (c) -0.3 – -0.1eV, and (d) -0.1 – 0.2eV, corresponding to the red, black, and blue boxes outlined in (e). A fixed isovalue of 0.002 e/Bohr^{-3} is used in all charge density plots. Silver-colored atoms represent Sn, brown for W, dark green for top Se, and light green for bottom Se. The black dashed lines in (b) are drawn along a high-symmetry direction of top Se atoms to illustrate the boundary periodicity, and the red arrows in (c) mark the center of a dislocation core positioned in the middle of a 7:6 periodic boundary segment as outlined by the red dashed lines perpendicular to the boundary. (e) Projected density of states (PDOS) plotted in histograms with the 0.1eV spacing, are compared across the center of each domain (top and bottom panels) and the different locations at boundary (center panel). (f-g) Atomic structure and morphology of 1T′-WSe_2/1T-$SnSe_2$ boundary: (f) STM image of 1T′-WSe_2/1T-$SnSe_2$ boundary (V_s=1.0V, I_t=100pA) with DFT simulated atomic structure overlaid on top. Yellow arrows mark the center of dislocation core. (g) Simulated STM image of the HS at 1V. The appearance of star-shaped features outlined by blue circles and their periodicity along boundary all match well with the STM image in (f). scale bars: 1nm.

To further comprehend the nature of boundary states and their correlation to the boundary structural configuration, STS was conducted along the boundary. Figure 2(c) reveals "acceptor-like" boundary states that arise near VBM, along with a state residing at ~0.65V. The "acceptor-like" states persist over the entire boundary, responsible for trapping electrons from the nearby domains, whereas the state at ~0.65V displays a modulated peak intensity along the boundary, correlating to the periodic boundary features observed in the inset (II). Due to the significant DOS contribution, boundary morphology cannot be atomically resolved. Nonetheless, as guided by lines drawn along the high symmetry direction of the hexagonal WSe_2 and $SnSe_2$ lattices (Fig. 3(a)), a 7:6 WSe_2 (red lines) to $SnSe_2$ (yellow lines) alignment was identified across the boundary, which translates into a boundary periodicity of ~2.3nm and implies the formation of misfit dislocations for relaxing the significant strain of ~15% between the two domains.[21, 22] Naturally, we suspect the electronic state arising at ~0.65V to be affiliated to misfit dislocations.

First-principles calculations of boundary morphology and electronic structures

To confirm our hypothesis, optimized 1H/1T boundary structure was calculated using density functional theory (DFT), which reveals the formation of dislocations centered on the (7:6) segment (Fig. 3(c)). To identify the associated electronic states, projected density of states (PDOS) were compared among various locations of the boundary as well as within the domain interiors (Fig. 3(e)). The three boundary states highlighted by the black, blue, and red boxes display drastically different real-space charge density distribution (Fig. 3(b-d)) that correlates well to the spatial modulation of the corresponding STS peaks observed in Fig. 2(c). Specifically, the boundary state enclosed

by the red box is dominated by misfit dislocations, and the two states marked by the black and blue boxes contain contribution from the entire boundary with the latter carrying a higher weight at dislocation cores (See more information in Section 3 and Fig. S3-S4 of ESI†).

Formation of misfit dislocations is expected to relax the strain at 1H/1T boundary.[21, 22] Since electron doping has already been excluded as the cause of phase transition, to address how the transition occurs we inspect its outcome, i.e., the 1T′-WSe_2:1T-$SnSe_2$ (1T′/1T) boundary. In Fig. 3(f), the optimized boundary structure calculated by DFT is overlaid on top of the STM image, which agrees with the simulated image (Fig. 3(g)) as highlighted by features surrounding the dislocation core (See more information in Section 4 of ESI†). It is worth noting that the periodicity of this boundary is identical to that of 1H/1T, owing to the same lattice parameter between the 1H and 1T′ phases of WSe_2 along the direction parallel to the boundary. Despite having the same periodicity, these two boundaries do exhibit some differences including the configuration of dislocation cores as marked by the arrows in Fig. 3(c) and (f), suggesting a relative gliding between the two domains during phase transition.

A new phase transition mechanism in core-shell architecture

Next, we review the different stages during the core-shell formation and propose a new phase transition mechanism. The observed phase transformation in WSe_2 core is closely related to the degree of $SnSe_2$ coverage surrounding WSe_2 islands. As shown in Fig. 1(b) and (f), no phase transition is observed in the initial stage when individual $SnSe_2$ domains developed from the adjacent 1H-WSe_2 edges are not yet merged, which is expected considering the relaxation of strain at the 1H/1T boundary by dislocations.[21, 22] With increasing coverage, $SnSe_2$ domains start to encounter each other and coalesce to form enclosed core-shell structures. During the dynamic process of merging (highlighted by light grey in Fig. 1(g)), rearrangement of lattices necessarily occurs as the result of lattice misalignment between $SnSe_2$ domains. The degree of freedom in the (7:6) registry arising from prior nucleation of $SnSe_2$ along 1H-WSe_2 edges, signified by the position of misfit dislocation (Fig. 4(a)), plays the major role in this lattice misalignment. Figure 4(b) illustrates the merging front (grey box) of type I and type II configurations, depicted in Fig. 4(a), from the right and bottom edges, respectively. Without considering the further contribution from boundary separation (Fig. S6 of ESI†), it translates into a ~13% lattice misalignment in the shell. With the various combinations of (7:6) configurations from the adjacent edges, the degree of lattice distortion in the shell could be even greater than that presented in Fig. 4(b).

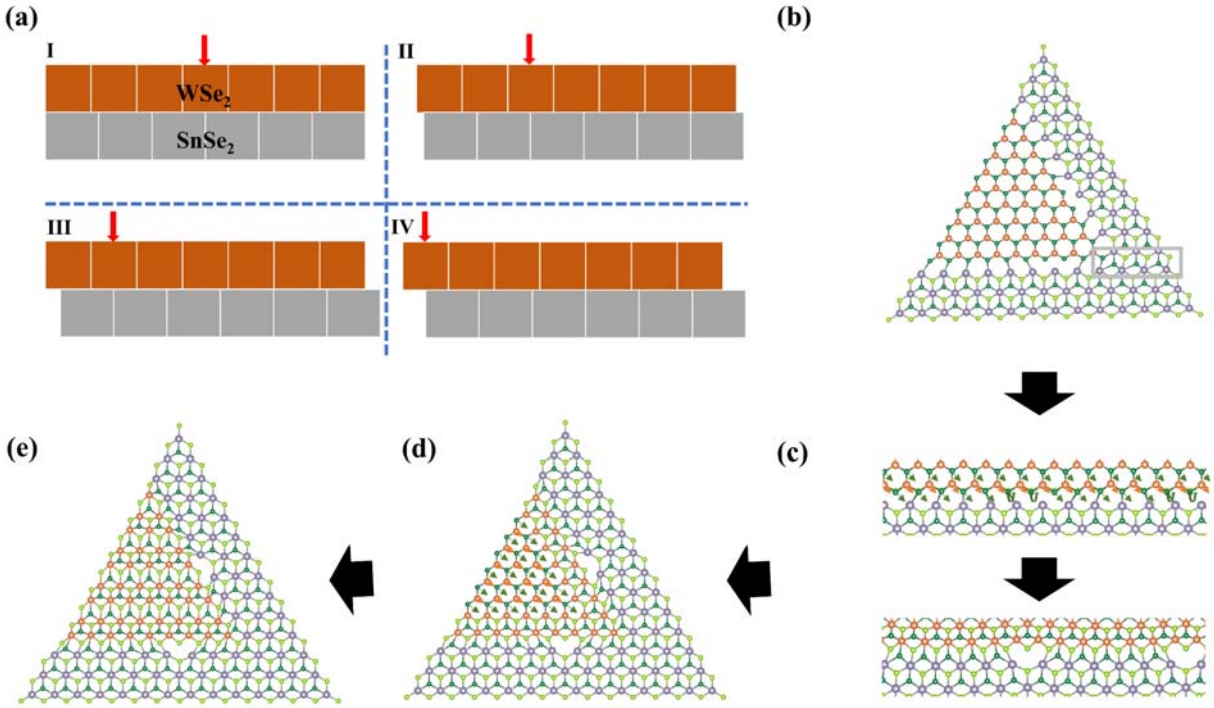

Figure 4. Mechanism of stress propagation for phase transformation of WSe_2. (a) Four different (7 WSe_2:6 $SnSe_2$) lattice alignment scenarios at 1H-WSe_2/1T-$SnSe_2$ boundary with the varying position of misfit dislocation (red arrow). (b) As $SnSe_2$ domains extended from adjacent WSe_2 edges merge, the random combination of (7 WSe_2:6 $SnSe_2$) pairs results in lattice misalignment at the merging front of the shell, highlighted in the grey box. The combination of type I and type II configurations from the right and bottom edges, respectively, is illustrated, which correlates to ~13% lattice misalignment (0.05nm/0.38nm) in the shell. (c) Rearrangement of $SnSe_2$ lattices during the coalescing induces a shear stress along the H-WSe_2/T-$SnSe_2$ boundary. The gliding motion of Se with respect to W, illustrated by the straight arrows, contributes to the polymorphic phase transformation of WSe_2. The curved arrows represent the possibility of Se atoms leaving the boundary. (d) Schematics to delineate the propagation of phase transformation from boundary to interior of WSe_2 until the entire WSe_2 island is transformed in (e). Note that for the purpose of illustrating stress propagation these schematics represent a simplified scenario where only two $SnSe_2$ domains from adjacent WSe_2 edges merge, whereas in actual experiments the complete WSe_2 phase transformation is often observed when WSe_2 islands are enclosed by $SnSe_2$ (Fig. 1(d)-(e)).

As $SnSe_2$ rearrange to reach the energetically favored positions, a shear stress is inevitably created along the covalently bonded $WSe_2/SnSe_2$ junctions. We speculate this stress to cause a gliding motion of Se atoms relative to W ions (Fig. 4(c)), which then propagates into the domain interior and leads to a H to T′ phase transition in WSe_2 (Fig. 4(d-e)). The dimerization of metal atoms in Fig. 4(e) is resulted from spontaneous structural relaxation of 1T phase due to Peierls-like distortion, which is a well-known phenomenon in group VI TMDs.[33] When WSe_2 islands are not yet fully enclosed by $SnSe_2$, a partial phase transition is induced (Fig. 1(h)), consistent with the experimental observation in Fig. 1(c). In the complete core-shell structure, the entire WSe_2 domain is transformed into the metastable T′-phase (Fig. 1(i), and (d-e)). This shell-induced gliding motion may be further facilitated by the symmetry of $SnSe_2$ shell as Se atoms at the merging front, where the gliding is initiated, are already adopting the T phase. Note that the collective structural transformation of $SnSe_2$ domains is unlikely to occur since there is no reported metastable phase in the nearby energy range.

Integration of phase transition with core-shell architecture is unique and potentially versatile as: (i) TMD core is less likely to suffer from structural damage, such as fracturing, in comparison to other stress-based phase-transition methods.[18, 34-36] H to T′ phase transition of group VI TMDs (MoS_2, WS_2, $MoSe_2$, WSe_2) requires a biaxial strain of ~10-15%.[16] It is difficult to sustain such a big strain via conventional heteroepitaxy. Formation of misfit dislocations, as evidenced along each individual 1H/1T boundaries in this study, will largely relax the epitaxial strain[21, 22]. When the strain is applied using more aggressive methods like hydrostatic pressure with diamond anvil cell,[34] e-beam,[35, 37] or tip pulling,[36] potential development of fractures and vacancies will become a concern. (ii) It is less susceptible to contaminations[19, 38] or other undesirable substrate effects[20] as in the charge-transfer based techniques that involve foreign dopants. (iii) The methodology is likely applicable to other TMDs with the proper choice of core and shell materials. Covalent bonding between core and shell is necessary to enable the stress propagation from shell to core. Meanwhile, to create sufficiently large lattice misalignment as shells coalesce, it is mandatory to select shell candidates that bear decent lattice mismatch with the core. (iv) Establishment of phase transition on van der Waals interacting substrates not only reduces the constrain on the choice of substrate, but also opens possibilities to extend the technique to other vapor deposition methods, such as chemical vapor deposition which holds promise on scalability (See more information in Section 6 of ESI†).[39]

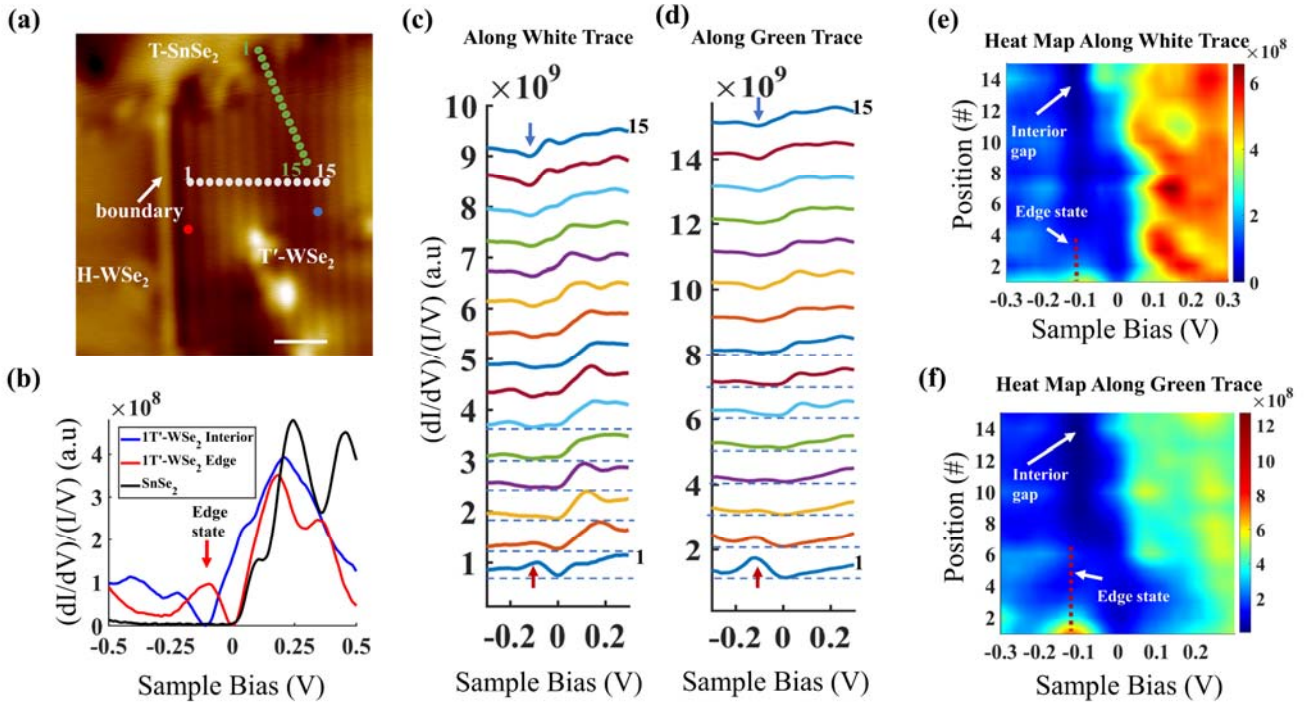

Figure 5. Topological edge state of 1T′-WSe_2. (a) STM image illustrating partially converted WSe_2 island (V_s=2V, I_t=30pA) on 1H-WSe_2/HOPG. The zoomed-out image of the same area is shown in Fig. 1(c). (b) Normalized dI/dV spectra (setpoint: V_s=0.5V, I_t=200pA) taken on the interior of 1T′-WSe_2 island (blue dot in (a)), the boundary (red dot in (a)), and $SnSe_2$, respectively. The blue curve reveals a dip at around -110mV which is associated with the bandgap of 1T′-WSe_2. Boundary (red) curve shows an edge state arising within the bandgap of 1T′-WSe_2 as well as the gap of $SnSe_2$ shell (black curve). (c-d) To examine the spatial extension of the edge state and to distinguish whether local structural perturbations influence this extension, dI/dV spectra are taken across both the smooth H- to T′-WSe_2 boundary (white trace in (a)) and the T′-WSe_2 to T-$SnSe_2$ boundary with periodic misfit dislocations (green trace in (a)). The red and blue arrows provide eye guide for the locations of the edge state and the interior bandgap, respectively. (e-f) DOS heat maps corresponding to (c) and (d), respectively. The extension of the edge state is drawn to the point where its DOS vanishes (red dashed lines), which corresponds to ~1.8nm for both boundaries. This demonstrates that the topological edge state is preserved in the core-shell architecture regardless of the boundary inhomogeneity and local perturbations associated with misfit dislocations. Scale bar: 2nm.

Topological properties of 1T′-WSe_2 core

Most importantly, realization of phase transition on the template of HSs allows the rational design and integration of TMD functionalities. Proximity coupling could further lead to the emergence of new phenomena and enable the exploration of new physics that is otherwise not accessible.[6] In the $WSe_2/SnSe_2$ core-shell architecture, 1T′-WSe_2 is expected to be a 2D TI,[11, 12] which holds immense potential for applications of quantum spin hall (QSH) effect due to its much larger bandgap (~120meV) with respect to 1T′-WTe_2 and its better chemical stability in comparison to other large bandgap QSH insulators like stanene.[33, 40, 41] To explore the effects of local defects on the extension of topological edge state, we investigate both 1T′-WSe_2/1H-WSe_2 (smooth) and 1T′-WSe_2/1T-$SnSe_2$ (containing periodic misfit dislocations) boundaries on a partially phase-converted domain shown in Fig. 1(c) and its zoom-in image in Fig. 5(a). As depicted in Fig. 5(b), a dip feature centered at ~ -110meV (blue curve) is observed on the interior of 1T′-WSe_2, whereas a conducting edge state (red curve) that is located right above the dip feature emerges near the boundary between 1T′-WSe_2 and a trivial semiconductor/insulator, i.e., 1H-WSe_2 or 1T-$SnSe_2$ in our study. The dip feature was suggested to be the consequence of gap reduction due to electron lifetime broadening associated with substrate coupling, vibrational, or electronic scattering.[11, 12] Spatial extension of the edge state was examined by taking STS spectra along the white and green dotted lines in Fig. 5(a), corresponding to the smooth and "rough" boundaries, respectively. As revealed in the vertically offset spectra as well as DOS heatmaps (Fig. 5(c)-(f)), this edge state penetrates ~ 1.8 nm into the interior of 1T′-WSe_2 at both boundaries, which provide strong evidence towards the preservation of extended edge state regardless of the boundary inhomogeneity and local perturbations (See more information in Section 7 of ESI†). The robustness of the extended edge state concurs with its topological nature. Finally, the as-grown 1T′-WSe_2/1T-$SnSe_2$ lateral HS provides a valuable platform for investigating proximity-induced superconductivity[14] on the topological edge of 1T′-WSe_2 when the system is cooled below the superconducting transition temperature (Tc = ~ 4.84K) of $SnSe_2$.[28] Topological superconductivity is a functional ingredient for realizing Majorana bound states, which hold great potential to implement topological qubits in fault-tolerant quantum computation.[15]

Conclusions

In conclusion, we successfully demonstrate a H to T′ phase transition on van der Waals interacting substrates based on the formation of $WSe_2/SnSe_2$ core-shell lateral HS. With comprehensive STM/STS and first-principles calculations, we propose a novel phase transition mechanism derived from shell to core stress propagation, which is presumably applicable to other TMDs and vapor deposition methods. In addition, we show that the topological edge state originating from 1T′-WSe_2 remains intact and is robust to periodic local perturbations at the core-shell boundary. $WSe_2/SnSe_2$ lateral HS with the directly exposed heterojunction provides a unique template for future investigations into proximity-induced superconductivity at the topological edge and the spatial extent of superconducting proximity effect.

Conflicts of interest

There are no conflicts to declare.

Acknowledgements

We acknowledge the financial support from the U.S. Department of Energy (DOE), Office of Basic Energy Sciences, Division of Materials Sciences and Engineering under Award Number DE-SC0019120.

Notes and references

1. M. Zeng, Y. Xiao, J. Liu, K. Yang and L. Fu, *Chem. Rev.*, 2018, **118**, 6236-6296.
2. S. H. Bae, H. Kum, W. Kong, Y. Kim, C. Choi, B. Lee, P. Lin, Y. Park and J. Kim, *Nat. Mater.*, 2019, **18**, 550-560.
3. A. L. Zhao, H. Li, X. J. Hu, C. Wang, H. Zhang, J. G. Lu, S. C. Ruan and Y. J. Zeng, *J. Phys. D Appl. Phys.*, 2020, **53**, 293002.
4. G. P. Neupane, K. Zhou, S. S. Chen, T. Yildirim, P. X. Zhang and Y. R. Lu, *Small*, 2019, **15**, 1804733.
5. K. L. Seyler, D. Zhong, B. Huang, X. Y. Linpeng, N. P. Wilson, T. Taniguchi, K. Watanabe, W. Yao, D. Xiao, M. A. McGuire, K. M. C. Fu and X. D. Xu, *Nano Lett.*, 2018, **18**, 3823-3828.
6. J. Wang and S. C. Zhang, *Nat. Mater.*, 2017, **16**, 1062-1067.
7. A. Splendiani, L. Sun, Y. B. Zhang, T. S. Li, J. Kim, C. Y. Chim, G. Galli and F. Wang, *Nano Lett.*, 2010, **10**, 1271-1275.
8. Y. Xiao, M. Y. Zhou, J. L. Liu, J. Xu and L. Fu, *Sci. China Mater.*, 2019, **62**, 759-775.
9. S. Wu, V. Fatemi, Q. D. Gibson, K. Watanabe, T. Taniguchi, R. J. Cava and P. Jarillo-Herrero, *Science*, 2018, **359**, 76-79.
10. S. J. Tang, C. F. Zhang, D. Wong, Z. Pedramrazi, H. Z. Tsai, C. J. Jia, B. Moritz, M. Claassen, H. Ryu, S. Kahn, J. Jiang, H. Yan, M. Hashimoto, D. H. Lu, R. G. Moore, C. C. Hwang, C. Hwang, Z. Hussain, Y. L. Chen, M. M. Ugeda, Z. Liu, X. M. Xie, T. P. Devereaux, M. F. Crommie, S. K. Mo and Z. X. Shen, *Nat Phys*, 2017, **13**, 683-687.
11. P. Chen, W. W. Pai, Y. H. Chan, W. L. Sun, C. Z. Xu, D. S. Lin, M. Y. Chou, A. V. Fedorov and T. C. Chiang, *Nat. Commun.*, 2018, **9**, 2003.
12. M. M. Ugeda, A. Pulkin, S. Tang, H. Ryu, Q. Wu, Y. Zhang, D. Wong, Z. Pedramrazi, A. Martin-Recio, Y. Chen, F. Wang, Z. X. Shen, S. K. Mo, O. V. Yazyev and M. F. Crommie, *Nat. Commun.*, 2018, **9**, 3401.
13. H. Yang, S. W. Kim, M. Chhowalla and Y. H. Lee, *Nat. Phys.*, 2017, **13**, 931-937.
14. L. Fu and C. L. Kane, *Phys. Rev. B*, 2009, **79,** 161408(R).
15. S. Das Sarma, M. Freedman and C. Nayak, *Npj Quantum Inform.*, 2015, **1,** 15001.
16. K. A. Duerloo, Y. Li and E. J. Reed, *Nat. Commun.*, 2014, **5**, 4214.
17. M. S. Sokolikova, P. C. Sherrell, P. Palczynski, V. L. Bemmer and C. Mattevi, *Nat. Commun.*, 2019, **10**, 712.

18. A. Apte, V. Kochat, P. Rajak, A. Krishnamoorthy, P. Manimunda, J. A. Hachtel, J. C. Idrobo, S. A. Syed Amanulla, P. Vashishta, A. Nakano, R. K. Kalia, C. S. Tiwary and P. M. Ajayan, *ACS Nano*, 2018, **12**, 3468-3476.
19. Y. Ma, B. Liu, A. Zhang, L. Chen, M. Fathi, C. Shen, A. N. Abbas, M. Ge, M. Mecklenburg and C. Zhou, *ACS Nano*, 2015, **9**, 7383-7391.
20. X. Yin, C. S. Tang, D. Wu, W. Kong, C. Li, Q. Wang, L. Cao, M. Yang, Y. H. Chang, D. Qi, F. Ouyang, S. J. Pennycook, Y. P. Feng, M. B. H. Breese, S. J. Wang, W. Zhang, A. Rusydi and A. T. S. Wee, *Adv. Sci.*, 2019, **6**, 1802093.
21. X. Zou, Y. Liu and B. I. Yakobson, *Nano Lett.*, 2013, **13**, 253-258.
22. H. P. Komsa and A. V. Krasheninnikov, *Adv Electron Mater*, 2017, **3,** 1600468.
23. W. Chen, X. D. Xie, J. Y. Zong, T. Chen, D. J. Lin, F. Yu, S. E. Jin, L. J. Zhou, J. Y. Zou, J. Sun, X. X. Xi and Y. Zhang, *Sci. Rep.*, 2019, **9,** 2685.
24. L. W. Liu, Z. Z. Ge, C. H. Yan, A. D. Moghadam, M. Weinert and L. Li, *Phys. Rev. B*, 2018, **98,** 235304.
25. D. Voiry, A. Mohite and M. Chhowalla, *Chem. Soc. Rev.*, 2015, **44**, 2702-2712.
26. Y. Wang, J. Xiao, H. Y. Zhu, Y. Li, Y. Alsaid, K. Y. Fong, Y. Zhou, S. Q. Wang, W. Shi, Y. Wang, A. Zettl, E. J. Reed and X. Zhang, *Nature*, 2017, **550**, 487-491.
27. C. Zhang, Y. Chen, A. Johnson, M. Y. Li, L. J. Li, P. C. Mende, R. M. Feenstra and C. K. Shih, *Nano Lett.*, 2015, **15**, 6494-6500.
28. Y. M. Zhang, J. Q. Fan, W. L. Wang, D. Zhang, L. L. Wang, W. Li, K. He, C. L. Song, X. C. Ma and Q. K. Xue, *Phys. Rev. B*, 2018, **98,** 220508(R).
29. W. T. Hsu, L. S. Lu, D. Wang, J. K. Huang, M. Y. Li, T. R. Chang, Y. C. Chou, Z. Y. Juang, H. T. Jeng, L. J. Li and W. H. Chang, *Nat. Commun.*, 2017, **8**, 929.
30. A. T. Hanbicki, M. Currie, G. Kioseoglou, A. L. Friedman and B. T. Jonker, *Solid State Commun.*, 2015, **203**, 16-20.
31. H. J. Liu, L. Jiao, L. Xie, F. Yang, J. L. Chen, W. K. Ho, C. L. Gao, J. F. Jia, X. D. Cui and M. H. Xie, *2D Mater.*, 2015, **2**, 034004.
32. T. Shimada, F. S. Ohuchi and B. A. Parkinson, *Jpn. J. Appl. Phys. 1*, 1994, **33**, 2696-2698.
33. X. Qian, J. Liu, L. Fu and J. Li, *Science*, 2014, **346**, 1344-1347.
34. A. P. Nayak, T. Pandey, D. Voiry, J. Liu, S. T. Moran, A. Sharma, C. Tan, C. H. Chen, L. J. Li, M. Chhowalla, J. F. Lin, A. K. Singh and D. Akinwande, *Nano Lett.*, 2015, **15**, 346-353.
35. S. Kretschmer, H. P. Komsa, P. Boggild and A. V. Krasheninnikov, *J. Phys. Chem. Lett.*, 2017, **8**, 3061-3067.
36. S. Song, D. H. Keum, S. Cho, D. Perello, Y. Kim and Y. H. Lee, *Nano Lett.*, 2016, **16**, 188-193.
37. Y. C. Lin, D. O. Dumcenco, Y. S. Huang and K. Suenaga, *Nat. Nanotechnol.*, 2014, **9**, 391-396.
38. Y. Q. Fang, Q. Dong, J. Pan, H. Y. Liu, P. Liu, Y. Y. Sun, Q. J. Li, W. Zhao, B. B. Liu and F. Q. Huang, *J. Mater. Chem. C*, 2019, **7**, 8551-8555.
39. H. Li, Y. Li, A. Aljarb, Y. Shi and L. J. Li, *Chem. Rev.*, 2018, **118**, 6134-6150.
40. Z. Y. Fei, T. Palomaki, S. F. Wu, W. J. Zhao, X. H. Cai, B. S. Sun, P. Nguyen, J. Finney, X. D. Xu and D. H. Cobden, *Nat. Phys.*, 2017, **13**, 677-682.
41. Y. Xu, B. Yan, H. J. Zhang, J. Wang, G. Xu, P. Tang, W. Duan and S. C. Zhang, *Phys. Rev. Lett.*, 2013, **111**, 136804.

